aerospace

MDPI

Article

A Comprehensive Visibility Assessment Method for Space-Based Optical Surveillance with Photometric and Detection Constraints

Jingyue Wan [1,2] and Desheng Liu [1,2,*]

[1] School of Space Information, Space Engineering University, Beijing 101416, China; w2118125605@163.com
[2] National Key Laboratory of Space Target Awareness, Beijing 101416, China
* Correspondence: liudesheng@hgd.edu.cn; Tel.: +86-15910624248

Abstract

Quantifying detectable observation opportunities for space-based optical surveillance constellations requires joint consideration of geometric visibility, target photometry, and detector performance. To this end, this paper proposes a three-layer progressive comprehensive visibility model that integrates geometry, photometry, and detection performance constraints. The model decomposes the entire physical process of optical detection and imposes multiple constraints sequentially: geometric limits involving Earth and atmospheric occultation, solar avoidance angle, and conical Earth shadow; photometric limits based on a two-component phase function combining diffuse and specular reflection; a continuous signal-to-noise ratio (SNR) model unified by equivalent pixel coverage for both point-source and streaked imaging, used for quantitative visibility judgment. A 144-h numerical simulation is conducted for a low-orbit surveillance constellation of four satellites, deployed on four evenly spaced 800 km sun-synchronous orbital planes, targeting geostationary Earth orbit (GEO) and low Earth orbit (LEO) objects. The results show that under the constellation configuration defined in this paper, GEO targets have long but sparse, discontinuous visible arcs with a comprehensive visibility rate of less than 10%. From the perspective of sequential screening, their visibility is mainly limited by photometric conditions; LEO targets exhibit a discrete short-peak distribution with a comprehensive visibility rate over 20%, which is jointly constrained by line-of-sight geometry and SNR. The proposed model effectively distinguishes geometric visibility from practical detectability, and lays a theoretical foundation for mission planning and resource scheduling of space-based optical surveillance systems.

Keywords: space-based optical surveillance; visibility analysis; SNR model; photometric constraint

Academic Editor: Hyun-Ung Oh

Received: 26 October 2026
Revised: 21 November 2026
Accepted: 23 November 2026
Published: 24 November 2026

Copyright: © 2026 by the authors. Licensee MDPI, Basel, Switzerland. This article is an open access article distributed under the terms and conditions of the Creative Commons Attribution (CC BY) license.

1. Introduction

Space situational awareness (SSA) is a core capability for strengthening space governance and ensuring the safety of space activities and space assets. With the explosive growth of global space activities, the number of on-orbit spacecraft and space debris has risen sharply, and the space orbital environment has become increasingly complex. This has created an urgent need for routine, high-precision, and wide-area surveillance of

space targets [1]. Compared with ground-based optical surveillance systems, space-based optical systems are free from the constraints of the day–night cycle, atmospheric turbulence, cloud cover, and geographical location. They can achieve continuous coverage of near-Earth space targets and offer significant advantages in detecting long-distance targets such as those in geostationary orbits. Therefore, they have become a key development direction for SSA systems [2]. As a fundamental component of constellation design, surveillance mission planning, and resource scheduling, the accuracy of visibility analysis directly determines the effectiveness of constellation design and the efficiency of mission execution [3]. In recent years, numerous constellation optimization design methods for space-based optical surveillance have been proposed, including constellation configuration optimization based on phase volume coverage and observation geometry quality index, preliminary analysis of optical surveillance constellations for LEO coverage, and weighted optimization approaches for large-scale LEO surveillance missions [4,5]. In all these studies, visibility analysis serves as the core basis for evaluating constellation performance. Existing studies on visibility analysis for space-based surveillance of space targets are predominantly centered on geometric constraints. They determine the visibility of a target to the payload solely based on constraints such as general geometric visibility between the target and the observation payload, target illumination constraints, and background illumination avoidance. These geometric constraints only reflect that sunlight reflected by the target reaches the sensor entrance pupil without obstruction, and do not imply that the target can be reliably detected by the sensor [6]. Both engineering practice and theoretical analyses indicate that factors including the optical reflection characteristics of the target surface, observation phase angle, deep space background radiation noise, as well as the sensor's intrinsic photoelectric conversion performance and exposure time, all exert significant influences on the final detection result [7–9]. Furthermore, research progress in the field of optical data simulation for space-based space situational awareness also shows that imaging modeling requires comprehensive consideration of the physical properties of various optical sensing systems, and that visibility analysis frameworks relying solely on geometric constraints can hardly meet the demands of increasingly refined surveillance missions [10].

In terms of geometric visibility modeling, conventional methods typically simplify the Earth as a standard sphere with its solid radius taken as the occlusion boundary, and employ a cylindrical Earth shadow model to determine the target illumination state. However, the Earth's dense atmosphere exerts significant absorption and scattering effects on optical signals traversing it, so using only the solid Earth radius as the occlusion boundary will introduce systematic errors. The cylindrical Earth shadow model assumes sunlight to be parallel rays and the Earth's shadow to be an infinitely long cylinder, ignoring the penumbra effect arising from the solar apparent diameter, which causes a maximum determination error of the Earth shadow boundary on the order of minutes. Previous studies have comprehensively incorporated multiple constraints such as Earth occultation, earthshine, Earth shadow, sunlight and moonlight to establish visibility prediction methods for space-based optical observation [11,12], yet their handling of the Earth occultation radius and Earth shadow boundary still relies on simplified assumptions, without fully considering the atmospheric attenuation effect and penumbra transition characteristics. A visibility region calculation method based on three-dimensional torus mapping has been proposed, which is capable of mapping disconnected visibility regions in a two-dimensional phase plane into closed three-dimensional curves [13]; however, it focuses on the geometric efficiency of coverage analysis and does not involve the issues of atmospheric occlusion and shadow accuracy. In addition, although the equal-probability group visibility criterion and the unified

https://doi.org/10.3390/aerospace13121106

visibility criterion simultaneously account for Earth occultation, sensor field of view and slant range constraints [14], they remain insufficient in terms of the physical refinement of geometric constraints. While these simplified treatments at the geometric level reduce computational complexity to some extent, the resulting determination errors cannot be neglected in refined surveillance missions.

In terms of target photometric characteristic modeling, the surface of realistic space targets is composed of various materials such as solar arrays, metal structures, and thermal control films, and their reflection characteristics typically incorporate both near-Lambertian diffuse reflection and highly directional specular reflection components. As a result, a single Lambertian model cannot accurately characterize the variation pattern of reflection intensity with the observation phase angle. Scholars have proposed a modeling method for the visible imaging characteristics of space targets based on the Bidirectional Reflectance Distribution Function (BRDF). By discretizing the target surface into grids and introducing the BRDF model to describe the light reflection properties of each grid, the modeling accuracy is effectively improved [15,16]. Studies evaluating the photometric impacts of different surface materials on LEO satellites using finite element modeling and the Ashikhmin–Shirley BRDF model indicate that high specular reflection produces more dramatic brightness variations and glints [17,18]; simulations of apparent magnitude curves for space targets of different shapes using an isotropic Phong BRDF model and an attitude quaternion update model reveal the combined effects of target spatial position, shape, and attitude on apparent magnitude [19]. Furthermore, a BRDF photometric model for Starlink satellites established based on photometric observation data [20] further confirms that refined photometric modeling is a critical step in enhancing the accuracy of visibility analysis. Nevertheless, the above studies focus on the intrinsic light scattering physical mechanism of the target itself, and fail to form a closed loop with the observation geometry link and detector performance.

In terms of detection capability evaluation, most existing analyses default to a static point source imaging mode for targets and fail to fully account for the streak imaging characteristics of high-speed moving LEO targets, resulting in significant deviations between SNR calculations and actual detection performance. For dim target detection under low SNR conditions, existing studies have proposed a faint space target detection method based on time-series images; by integrating an SNR enhancement algorithm with an adaptive background noise suppression algorithm, this method achieves a high detection probability and a low false alarm probability at an SNR level of 3 [21]. To address the difficulty in detecting point-like space targets under short exposure conditions, a modular detection framework consisting of candidate region selection, support vector machine (SVM) classification, motion decomposition and trajectory correction has been proposed [22]. Regarding the streak imaging mode of LEO targets, relevant studies indicate that the high-speed motion of targets causes optical signals to spread across multiple pixels on the focal plane, and a refined effective magnitude model and a bright pixel grayscale model based on the Gaussian point spread function (PSF) have been developed accordingly [23,24]. For dim streak-like space targets, an improved matched filtering detection method based on anisotropic Gaussian kernels and directional consistency analysis has been proposed, which effectively reduces the false alarm rate [25]. These studies collectively demonstrate that detector performance imposes a hard constraint on detectability, and neglecting imaging mode differences and detection threshold limitations will lead to severe distortion of visibility assessment results.

Previous studies have incorporated target photometry and detector performance into optical detectability assessment. Shell [26] developed a radiometric model accounting for diffuse and specular reflection, sensor response, noise, and image motion, and evaluated ground-based GEO/LEO sensing and GEO-based GEO sensing. Campiti et al. [27]

combined orbital geometry, illumination constraints, photometric modeling, image motion, and SNR evaluation to assess onboard star trackers' ability to detect potentially colliding LEO objects, including detection probability and potential orbit-determination benefits. Building on these studies, the present work focuses on constellation-level observation opportunities and their limiting constraints for representative GEO and LEO targets observed by a LEO constellation.

For constellation-level assessment, evaluating target detectability at individual epochs needs to be complemented by the aggregation of observation windows and temporal coverage metrics. Furthermore, distinguishing rejection fractions along the screening sequence from the marginal effects of individual constraints helps identify the factors limiting detectable observation opportunities under a given constellation and payload configuration.

To address the aforementioned issue, this paper proposes a progressive visibility analysis model that integrates geometric constraints, target photometry, and payload detection capability. In the geometric layer, we introduce an effective occultation radius as an engineering approximation for atmospheric exclusion and adopt a conical Earth shadow model with conservative illumination screening. In the photometric layer, we construct a two-component phase function combining diffuse and specular reflection and establish an equivalent apparent magnitude system for quantitative brightness evaluation. In the detection capability layer, we establish a unified continuous SNR model governed by equivalent pixel coverage on the focal plane. The covered pixel count accounts for relative angular motion during the exposure and the sensor's instantaneous field of view, which naturally transitions from point-source-like to streaked imaging conditions without discrete mode switching, enabling quantitative assessment of detection performance for targets in different orbits. Using a four-satellite LEO sun-synchronous constellation with four evenly spaced orbital planes as the observation platform, we conduct simulation experiments for two representative GEO targets and two representative LEO targets. The temporal visibility patterns, evolution of key physical quantities, and sequential rejection fractions and marginal effects of individual constraints are systematically analyzed for both target types, thereby providing a quantitative assessment of detectable observation opportunities and their limiting factors under the selected simulation conditions.

2. Comprehensive Visibility Analysis Model

The proposed comprehensive visibility analysis model adopts a three-layer progressive architecture—geometry, photometry, and detection capability. The underlying design rationale stems from a complete decomposition of the physical process of optical detection of space targets. Physically, the optical detection of space targets must sequentially satisfy three conditions:

- The sunlight reflected by the target can reach the sensor's entrance pupil without occlusion.
- The received signal energy is strong enough to be perceivable by the photoelectric conversion device.
- The sensor's photoelectric conversion and electronic systems can, with sufficient confidence, extract the signal from the inherent noise background.

These three conditions constitute a complete physical causal chain; failure of any link would render the target "practically undetectable". Based on this understanding, this paper decomposes the visibility criterion into a logical AND operation with three inputs, each corresponding to a quantitative judgment of one of the above three physical links. The overall architecture of the proposed model is illustrated in Figure 1.

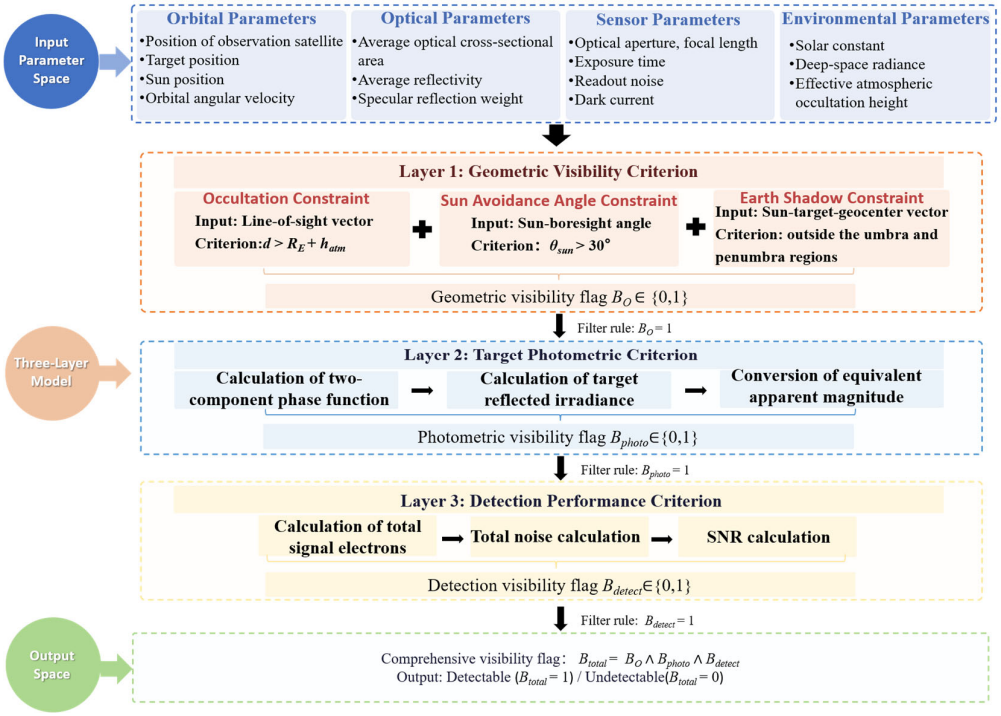

Figure 1. Overall architecture of the model.

2.1. Geometric Visibility Criterion

Geometric visibility is the basic premise for space-based optical detection. Unlike ground-based observation, in space-based observation both the target and the observer are in orbit and move at high speed, introducing more numerous and more complex geometric factors. Any effective observation must first ensure that the line of sight between the target and the observer is unobstructed, while also satisfying solar avoidance and solar illumination conditions [9,28]. As shown in Figure 2, let the position of the observation satellite be *S*, the position of the target be *T*, the position of the Sun be *O*, the Earth radius be R_E. In the J2000 geocentric equatorial coordinate system, at a given moment, the position vector of the Sun is $\boldsymbol{r}_o$, the position vector of the observation satellite is $\boldsymbol{r}_s$, and the position vector of the target satellite is $\boldsymbol{r}_t$.

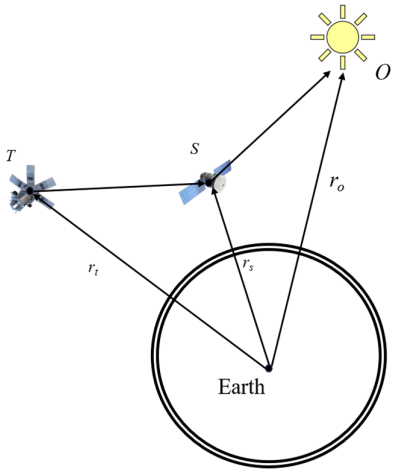

Figure 2. Geometric relationship among target, observation platform, Earth and Sun.

2.1.1. Earth Occultation Constraint

Earth occultation is the most fundamental geometric constraint, requiring that the line of sight between the target and the observer is not blocked by the Earth or its surrounding dense atmosphere. Traditional analysis methods usually take only the Earth's solid radius as the occultation boundary. This simplification ignores the significant absorption and scattering effects of the Earth's atmosphere on optical signals passing through it, and also fails to consider the impact of airglow on the detection payload. In fact, the dense atmosphere below 100 km altitude is sufficient to cause severe attenuation of optical signals passing through this region. Therefore, in the visibility analysis for space-based optical observations, it is insufficient to consider only the occultation effect of the solid Earth; the dense atmosphere must also be regarded as an effective occultation factor.

To this end, we define an effective occultation radius $R_{eff} = R_E + H_{atm}$, where H_{atm} is the effective atmospheric occultation height. Based on the vertical distribution of atmospheric optical depth, we set H_{atm} = 100 km, that is, when the line of sight passes through the atmosphere below 100 km altitude, the target light is attenuated to a level below the effective detection threshold (as shown in Figure 3). Given that both the observation satellite and the space target operate in orbits beyond the effective occultation radius, and both endpoints of the line-of-sight segment lie outside the occluding sphere, the shortest perpendicular distance from the line of sight to the geocenter is directly adopted as the occlusion criterion. The Earth and atmospheric occultation criterion is then given as follows: the shortest distance h_{min} from the line of sight to the geocenter must be greater than the effective occultation radius. The value of h_{min} can be directly obtained from the triangle area formula as follows:

$$h_{min} = \frac{\left\| \boldsymbol{r}_s \times \boldsymbol{r}_t \right\|}{\left\| \boldsymbol{r}_t - \boldsymbol{r}_s \right\|} \tag{1}$$

The unit vector along the line-of-sight direction is defined as

$$\boldsymbol{e}_{los} = \frac{\boldsymbol{r}_t - \boldsymbol{r}_s}{\| \boldsymbol{r}_t - \boldsymbol{r}_s \|} \tag{2}$$

Then the scalar parameter corresponding to the foot of the perpendicular from the geocenter to the line-of-sight straight line is given by

$$p = -\frac{\boldsymbol{r}_s \cdot \boldsymbol{e}_{los}}{\| \boldsymbol{r}_t - \boldsymbol{r}_s \|} = -\frac{\boldsymbol{r}_s \cdot (\boldsymbol{r}_t - \boldsymbol{r}_s)}{\| \boldsymbol{r}_t - \boldsymbol{r}_s \|^2} \tag{3}$$

The revised Earth occultation judgment rule is formulated as follows:

If $p \in [0,1]$, the foot of the perpendicular lies on the line-of-sight segment, and the occultation criterion is $h_{min} > R_{eff} = R_E + H_{atm}$;

If $p \notin [0,1]$, the foot of the perpendicular falls outside the line-of-sight segment, and the line of sight is inherently free from Earth occultation.

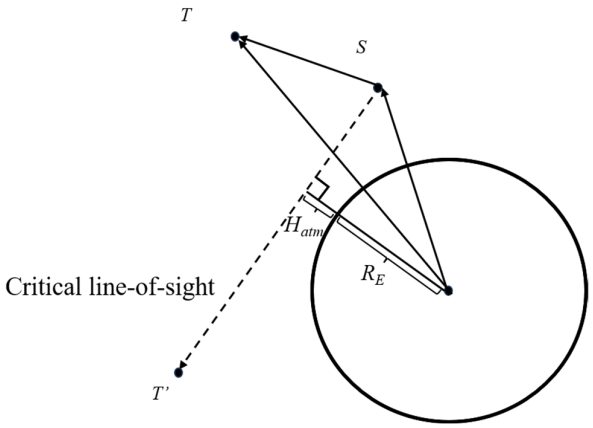

Figure 3. Earth occultation condition.

2.1.2. Solar Avoidance Angle Constraint

To achieve effective optical observation of space targets, the target itself cannot be located on or near the solar disk. If the target is too close to the Sun, intense direct sunlight will enter the sensor's optical system. This may cause detector saturation or even damage. Moreover, the resulting stray light and scattered background light will sharply reduce the contrast of the target signal, making the target completely submerged in the bright solar background and unrecognizable. Therefore, the solar avoidance angle constraint must be considered in geometric visibility analysis, i.e., the angle between the Sun direction and the sensor line of sight must be no less than a specified threshold (as shown in Figure 4). Let the angle between the Sun direction and the sensor line of sight be θ_{sun}; the constraint is then expressed as

$$\theta_{sun} = \arccos\frac{(\boldsymbol{r}_t - \boldsymbol{r}_s)\cdot(\boldsymbol{r}_o - \boldsymbol{r}_s)}{\|\boldsymbol{r}_t - \boldsymbol{r}_s\|\|\boldsymbol{r}_o - \boldsymbol{r}_s\|} \geq \theta_{sun,min}, \tag{4}$$

Following the typical design specifications of space-based optical surveillance systems, we set the threshold $\theta_{sun,min} = 30^{\circ}$. This threshold protects the detector from saturation while providing sufficient angular separation between the target and the Sun.

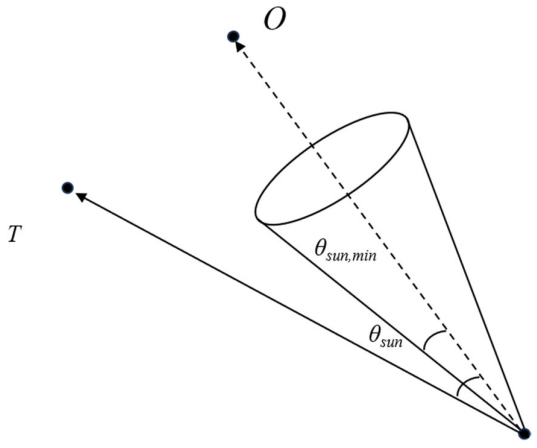

Figure 4. Solar avoidance angle condition.

2.1.3. Moon Avoidance Angle Constraint

For effective optical observation of space targets, the target itself must not lie within or near the lunar apparent disk. If the target is too close to the lunar direction, the intense sunlight reflected by the Moon will enter the sensor optical system. On one hand, it will raise the baseline of the detector background noise; on the other hand, the resulting stray light will significantly reduce the contrast of the target signal, causing the target to be submerged in the lunar stray light background and difficult to identify. Accordingly, the Moon avoidance angle constraint must be considered in geometric visibility analysis, requiring that the angle between the lunar direction and the sensor line of sight be no less than a certain threshold. Let the angle between the lunar direction and the sensor line of sight be θ_{moon}, and the position vector of the Moon be $\boldsymbol{r}_m$; this constraint is formulated as

$$\theta_{moon} = \arccos\frac{(\boldsymbol{r}_t - \boldsymbol{r}_s)\cdot(\boldsymbol{r}_m - \boldsymbol{r}_s)}{\|\boldsymbol{r}_t - \boldsymbol{r}_s\|\|\boldsymbol{r}_m - \boldsymbol{r}_s\|} \geq \theta_{moon,min} \tag{5}$$

The apparent radiance of the Moon is far lower than that of the Sun. The full Moon has an apparent magnitude of approximately −12.7, roughly 14 magnitudes fainter than the Sun's apparent magnitude of −26.7, which corresponds to a difference of about 400,000 times in incident irradiance. As a result, the threshold for the Moon avoidance angle is significantly smaller than that for the Sun avoidance angle. With reference to the typical design specifications of space-based optical surveillance systems, this paper sets the threshold at $\theta_{moon,min} = 10^{\circ}$. This threshold can suppress the interference caused by lunar stray light while retaining sufficient observable sky area for targets.

2.1.4. Earth Shadow Condition Constraint

Space targets themselves do not emit light. The prerequisite for optical detection is that the target must be illuminated by sunlight and reflect it into the sensor's field of view. Traditional analysis methods generally use a cylindrical Earth shadow model to judge whether the target lies in the Earth's shadow. The cylindrical model assumes that sunlight consists of parallel rays and that the Earth's shadow is an infinitely long cylinder. This assumption ignores the penumbral effect caused by the Sun's apparent diameter, resulting in a shadow boundary determination error on the order of minutes. To improve accuracy, we adopt a more accurate conical Earth shadow model. The conical model divides the Earth's shadow region into two parts: the umbra (receiving no direct sunlight) and the penumbra (receiving only partially blocked sunlight), as shown in Figure 5. The half-angles of the Earth's umbral cone and penumbral cone are given respectively by

$$\alpha_1 = \arcsin\left(\frac{R_O - R_E}{d}\right), \quad \alpha_2 = \arcsin\left(\frac{R_O + R_E}{d}\right), \tag{6}$$

where the solar radius is $R_O = 6.96 \times 10^5$ km, and the average Sun–Earth distance is $d = 1.496 \times 10^8$ km.

Define the unit vector pointing from the geocenter to the Sun as $\boldsymbol{e}_{sun} = \frac{\boldsymbol{r}_O}{\|\boldsymbol{r}_O\|}$, by decomposing the target along the Sun–Earth axis, the axial projection distance of the target z (positive on the sunlit side and negative on the shaded side) and the perpendicular distance from the target to the Sun–Earth axis ρ are derived:

$$z = \boldsymbol{r}_t \cdot \boldsymbol{e}_{sun}, \quad \rho = \sqrt{\boldsymbol{r}_t^{\,2} - z^2}, \tag{7}$$

The Earth shadow region lies on the shaded side of the Earth $z < 0$. At the target's axial position, the cross-sectional radii of the umbra and penumbra are respectively:

https://doi.org/10.3390/aerospace13121106

$$r_1(z) = R_E - \alpha_1 \cdot |z|, \quad r_2(z) = R_E + \alpha_2 \cdot |z| \tag{8}$$

In this paper, the penumbra region is also treated as having no effective illumination. A target is determined to be under Earth shadow occlusion when it lies on the shaded side and satisfies $\rho \le r_2(z)$; otherwise, it is in an illuminated state. The illumination flag of the target is defined as

$$illum = \begin{cases} 0, z < 0 \ and \ \rho \le r_2(z) \\ 1, others \end{cases} \tag{9}$$

Combining all the above conditions, the geometric visibility flag $B_O = 1$ if and only if earth occultation constraint and Equation (4) hold simultaneously and Equation (9) evaluates to 1.

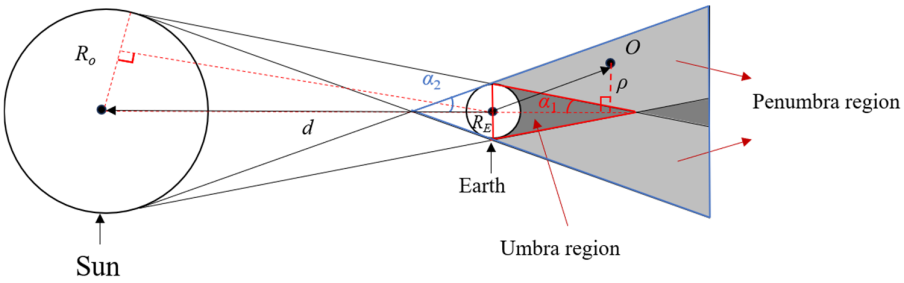

Figure 5. Earth shadow condition.

2.2. Target Photometric Criterion

This section constitutes the second layer of the comprehensive visibility model: the photometric calculation and pre-screening layer. Building on the output of the geometric visibility criterion, it quantitatively calculates the optical radiation intensity reflected by the target under the premise of unobstructed line of sight, and implements pre-engineering coarse screening via the limiting magnitude. This enables rapid elimination of targets far below the detection limit, thereby reducing the computational load for subsequent precise SNR determination. Physically, the directional reflection characteristics of the target surface can be finely characterized by the BRDF. However, BRDF is a multi-dimensional angular function dependent on both incident and reflection directions. The required surface material and structural parameters are difficult to obtain in large-scale orbital target screening scenarios, and angle-by-angle calculation incurs high computational overhead, making it hard to meet the demand for fast traversal computation [29]. For this reason, instead of directly adopting the BRDF model, this section employs a one-dimensional phase function derived from the spherical integration of BRDF. Defining the Sun–target–observer angle as the phase angle, this function depends exclusively on the phase angle and can be regarded as a statistical approximation of BRDF under far-field observation conditions when the target is approximated as a spherically symmetric body [28]. On this basis, this section introduces an equivalent apparent magnitude system to quantitatively characterize target brightness, and constructs a preliminary fast screening criterion for target photometry.

2.2.1. Irradiance Reflected by the Target

In the current mainstream parametric modeling framework for optical characteristics of space targets, complex-shaped space targets are usually approximated as ideal Lambertian diffusers with an average optical cross-section A_c and average reflectivity ρ

for computational simplicity [16]. This approximate model can provide statistical estimates of light-scattering characteristics that meet engineering requirements for large-scale applications such as orbit screening. However, the surfaces of real space targets consist of various materials including solar panels, metal structures, and thermal control coatings. Their reflection characteristics generally contain both near-Lambertian diffuse reflection and highly directional specular reflection components. A single Lambertian model cannot accurately describe the variation in reflection intensity with the observation phase angle. To address this problem, we adopt a two-component phase function constructed as a linear combination of diffuse and specular reflection components:

$$\Phi(\beta) = (1-k)\Phi_{diff}(\beta) + k\Phi_{spec}(\beta), \mathrm{k} \in [0,1], \tag{10}$$

where $\beta = \arccos\frac{(\boldsymbol{r}_t - \boldsymbol{r}_s)\cdot(\boldsymbol{r}_t - \boldsymbol{r}_o)}{\|\boldsymbol{r}_t - \boldsymbol{r}_s\|\|\boldsymbol{r}_t - \boldsymbol{r}_o\|}$, $\Phi_{diff}(\beta)$ and $\Phi_{spec}(\beta)$ denote the normalized diffuse and specular reflection phase functions, respectively. The parameter k represents the energy weight of the specular reflection component. Since different space targets have different surface materials, their corresponding k values vary. Without loss of generality, we set $k = 0.3$ in this paper.

Based on Lambert's cosine law and the integral formula for spherical radiant flux in radiometry, the normalized reflection intensity of an isotropic ideal diffuse sphere at phase angle β is given by

$$\Phi_{diff}(\beta) = \frac{1}{\pi}[\sin\beta + (\pi - \beta)\cos\beta] \tag{11}$$

This function is derived by integrating Lambert's law over spherical surface elements. When parallel light irradiates the sphere along the -z direction and the observation direction corresponds to phase angle β, the above closed-form expression can be obtained by integrating the reflected radiance per unit projected area over the hemispherical space. The boundary conditions are $\Phi_{diff}(0) = 1$, $\Phi_{diff}(\pi) = 0$, and the function decreases monotonously as β increases.

The target surface consists of a large number of microscopic surface elements, among which smooth surface elements produce a specular reflection component with pronounced directionality. The radiation intensity of this component peaks at the phase angle $\beta = 0$ and decays rapidly in a Gaussian profile as β increases. To ensure physical rationality while controlling computational complexity, this paper adopts a Gaussian specular reflection phase function:

$$\Phi_{spec}(\beta) = \exp(-\frac{\beta^2}{2\sigma^2}), \tag{12}$$

where $\sigma > 0$ is the characteristic angular parameter related to the microscopic surface roughness, representing the standard deviation of the Gaussian distribution of micro-facet normal directions. A smaller σ corresponds to more concentrated specular reflection energy, a sharper specular reflection lobe, and a smoother surface; a larger σ leads to more dispersed reflection energy, a broader reflection lobe, and a tendency toward diffuse reflection. In this paper, σ is set to 0.3. This function satisfies $\Phi_{spec}(0) = 1$ and decays rapidly with increasing β when the phase angle β deviates far from 0°, which is physically equivalent to the reflective directionality function when the micro-facet normal distribution follows an isotropic Gaussian distribution.

The average solar irradiance reaching the target in the visible band is denoted as $E_{sun,vis}$. Given the solar constant S = 1361 W/m² and an energy fraction of approximately

43% for the visible band, we obtain $E_{sun,vis}$ = 585 W/m² [30]. The total solar radiant power incident on the target is given by $E = \rho A_c E_{sun,vis}$, where ρ is the hemispherical directional reflectance and is set to 0.38 in this paper; Ac is the mean optical cross-sectional area, taken as 1.3 m². At the observation platform located at a distance $R = \|\boldsymbol{r}_t - \boldsymbol{r}_s\|$ from the target, the reflected irradiance is given by

$$E_{det} = E_{sun,vis} \cdot \frac{\rho A_c}{\pi R^2} \cdot \Phi(\beta) \tag{13}$$

2.2.2. Equivalent Apparent Magnitude

To correlate with the performance indicators of optical sensors, the physical irradiance Edet needs to be converted into the apparent magnitude system widely used in astronomy [31,32]. According to Pogson's law, the ratio of irradiance produced by two celestial bodies and their magnitude difference satisfy the following relation:

$$\frac{E_1}{E_2} = 10^{-0.4(m_1 - m_2)} \tag{14}$$

Taking the Sun as the reference source, its apparent magnitude $m_{sun} = -26.74$, and its visible irradiance is $E_{sun,vis}$. Denoting the target's apparent magnitude as m_v, we have

$$\frac{E_{det}}{E_{sun,vis}} = 10^{-0.4(m_v + 26.74)}, \tag{15}$$

solving for m_v:

$$m_v = -26.74 - 2.5\log_{10}\left(\frac{E_{det}}{E_{sun,vis}}\right), \tag{16}$$

By substituting the relevant parameters, we obtain the magnitude formula directly expressed by the geometric optical parameters of the target, observation distance and phase angle:

$$m_v = -26.74 - 2.5\log_{10}\left(\frac{\rho A_c \Phi(\beta)}{\pi R^2}\right), \tag{17}$$

Here, the Sun–Earth distance is assumed to be one standard astronomical unit, and its slight fluctuation is neglected since it exerts negligible influence on solar irradiance.

2.2.3. Model Benchmark Verification

To verify the numerical reliability of the photometric model, publicly available on-orbit satellite measurement data are selected for cross-validation. The verification subject is the ONEWEB-0176 satellite from the OneWeb constellation [32]. This sample is under a diffuse-reflection-dominated conventional observation state with no obvious specular glint, making it suitable for validating the statistical average model proposed in this paper. According to the satellite geometry and material parameters provided in the reference: the equivalent area of the main body and dual solar panels A_e = 3.0 m², the weighted average diffuse reflectance ρ_e = 0.08, the observation slant range R_{os} = 1.35 × 10⁶ m, and the observation phase angle β = 70°. The above parameters are substituted into Equations (10)–(17) successively for stepwise calculation.

First, the diffuse and specular reflection phase function components are calculated by Equation (11) and Equation (12) respectively:

$$\Phi_{diff} = \frac{1}{\pi}\left[\sin\left(\frac{7}{18}\pi\right) + \left(\pi - \frac{7}{18}\pi\right)\cos\left(\frac{7}{18}\pi\right)\right] \approx 0.508, \tag{18}$$

$$\Phi_{spec} = \exp[-\frac{(7\pi/18)^2}{2\times(0.3)^2}] \approx 0.00025\,, \tag{19}$$

The total phase function is synthesized according to Equation (9) with a specular weight $k = 0.3$:

$$\Phi(\beta) = (1-k)\cdot\Phi_{diff}(\beta) + k\cdot\Phi_{spec}(\beta) = 0.356\,, \tag{20}$$

Substituting the total phase function into Equation (13), the target reflected irradiance received at the observation platform is calculated as

$$E_{sc} = \frac{E_{sun}\cdot\rho_e\cdot A_e\cdot\Phi(\beta)}{\pi\cdot R_{os}^2} \approx 8.71\times10^{-12}\,W/m\,, \tag{21}$$

Finally, with the Sun as the reference source, the equivalent apparent magnitude of the target is calculated by Equation (16):

$$m = -26.74 - 2.5\lg\left(\frac{8.71\times10^{-12}}{585}\right) \approx 7.83\,, \tag{22}$$

The absolute deviation between the above calculation result and the measured magnitude of 8.10 mag at the same moment in the reference is 0.27 mag, which falls within the reasonable error range of engineering statistical models for space-based space target photometry. This deviation mainly stems from the engineering approximation of the spherically symmetric phase function in this paper to the asymmetric geometric structure of satellites, as well as the inherent parameter differences between the adopted material reflectance and that of the actual measured target. For statistical models oriented to large-scale orbital target screening, the accuracy of order-of-magnitude consistency and variation trend is more critical than single-point precision, and the current accuracy already satisfies the application requirements of visibility analysis.

2.2.4. Photometric Criterion

To improve computational efficiency in large-scale target scenarios, this paper introduces the limiting magnitude as the threshold for preliminary photometric coarse screening. It is designed to rapidly eliminate targets with excessive distances, extreme phase angles, and significantly insufficient reflected signals, so as to reduce the computational overhead of subsequent high-precision SNR calculations. Given the limiting magnitude of the sensor system m_{lim}, the photometric criterion is defined as the following Boolean condition:

$$B_{photo} = \begin{cases} 1, m_v \le m_{lim} \\ 0, m_v > m_{lim} \end{cases}, \tag{23}$$

This criterion promptly filters out undetectable targets whose reflected signals are too weak—due to large distance, unfavorable phase angles, or insufficient reflective area—at very low computational cost. In the subsequent simulation scenarios, we set m_{lim} = 13.5 according to the parameters of the sensor used.

2.3. Detection Performance Criterion

Whether a space target can be reliably detected by an optical sensor depends not only on its geometric visibility and apparent photometry, but also on whether the sensor can extract the target signal from the noise background with sufficient confidence within a limited exposure time. The signal–noise coupling model established in this section enables quantitative evaluation of target detectability via the SNR threshold criterion [33].

2.3.1. Basic Assumptions and Imaging Regimes

In space-based optical detection, the relative velocities between targets and observation satellites vary drastically, resulting in entirely different energy distributions of target images on the detector. The more dispersed the energy, the higher the total noise and the lower the SNR. Therefore, two typical regimes can be identified according to the degree of image motion. Let the focal length of the optical system be f and the pixel size be p. The instantaneous field of view corresponding to a single pixel is $\theta_{pix} = p/f$. Let the angular velocity of the target relative to the sensor be $\hat{\theta}$ and the exposure time be τ. The dimensionless image motion coefficient is defined as

$$N_{motion} = \frac{\hat{\theta}\tau}{\theta_{pix}} = \frac{f\hat{\theta}\tau}{p}, \tag{24}$$

this parameter represents the number of pixels traversed by the target image on the detector focal plane during exposure:

Point-source regime ($N_{motion} << 1$): The image motion of the target within the exposure time is far smaller than one pixel. Almost all radiant energy from the target is confined within the Airy disk defined by the point spread function (PSF) of the optical system, which can be equivalent to stationary point-source imaging. This mode typically corresponds to GEO targets. Since the relative angular velocity between the observation platform and GEO targets is extremely small, $N_{motion} << 1$ is maintained even with a long exposure time.

Streak regime ($N_{motion} >> 1$): The displacement of the target during exposure is much larger than a single pixel. The target's radiant energy spreads along the direction of motion and forms continuous trailing streaks on the focal plane. The length of the streak is proportional to N_{motion}, and energy disperses along the motion direction. Imaging of LEO targets generally falls into this regime.

In practice, the transition between point-like and streak-like imaging is a gradual physical process with no strict critical threshold. To avoid artificial discontinuity, this work adopts a unified continuous pixel-count model based on PSF convolution for all values of N_{motion}, as detailed in Section 2.3.3.

2.3.2. Number of Signal Photoelectrons

The total number of photoelectrons received by the detector depends only on the total incident radiant power, the light-gathering capacity of the optical system, the exposure time and the photoelectric conversion efficiency of the detector, and is independent of the imaging mode. Let the irradiance generated by the target at the entrance pupil of the sensor be E_{det}, and the effective light-collecting area of the optical system be $A_{opt} = \pi D^2 / 4$, where D denotes the effective aperture of the optical camera. Within the exposure time τ, the total radiant energy incident on the detector is $\tau E_{det} A_{opt}$.

The total number of signal photoelectrons S accumulated by the target signal on the detector is given by the photoelectric conversion equation:

$$S = Q \cdot \tau_{opt} \cdot \frac{\tau E_{det} A_{opt}}{h\nu} = Q \cdot \frac{\pi D^2}{4} \cdot \tau \cdot \frac{\lambda}{hc} \cdot \tau_{opt} \cdot E_{det}, \tag{25}$$

where Q denotes the detector quantum efficiency; τ denotes the exposure time; λ denotes the central wavelength of the detection band; h is Planck's constant, $6.626 \times 10^{-34} J \cdot s$; c is the speed of light in vacuum, $3 \times 10^8 m/s$; τ_{opt} represents the total

transmittance of the optical system. The above formula describes the physical process in which the total incident photon flux generates photoelectrons after attenuation by the optical system and conversion by the detector. It should be emphasized that this formula yields the total signal electron count, which remains constant regardless of whether the target energy is concentrated on a small number of pixels or dispersed across numerous pixels. Nevertheless, when calculating the SNR, the total system noise is directly correlated with the number of pixels covered by the target image. Accordingly, the number of pixels covered by the target image n_{ip} will be calculated separately in the following sections.

2.3.3. Unified Model for Number of Pixels Covered by Target Image

Let the tangential velocity of the target relative to the sensor be v_t and the range be d_{os}. The relative angular velocity is expressed as $\hat{\theta} = v_t / d_{os}$. During the exposure time, the angular displacement of the target on the image plane is $\Delta\theta = \hat{\theta}\tau$, and the corresponding linear displacement is $\Delta y = f\Delta\theta$. Given the pixel size p, the number of pixels over which the target image drifts on the image plane is

$$N_{motion} = \frac{f\hat{\theta}\tau}{p} = \frac{fv_t\tau}{pd_{os}}, \tag{26}$$

The target image is formed by the convolution of the optical system point spread function (PSF) with the motion trajectory. When the image motion is sufficiently small, the target appears as a static point source; as the motion increases, the image stretches along the motion direction and evolves into an elongated streak.

For a diffraction-limited system, the linear radius of the first dark ring of the Airy disk is $r_{airy} = 1.22\lambda F$, where $F = f/D$ denotes the focal ratio. Under the adopted optical parameters, the diffraction-limited PSF is much smaller than a single pixel. Considering optical aberrations, sampling design and sub-pixel positioning accuracy, a conservative engineering value for the static point-source coverage is adopted:

$$n_{ip,point} = 4, \tag{27}$$

which corresponds to an equivalent 2 × 2 pixel spot, with an effective PSF width of 2 pixels.

Based on the convolution area of the static PSF along the motion trajectory, a unified continuous pixel-count model is established for all motion conditions, which eliminates the artificial discontinuity caused by hard-threshold mode switching:

$$n_{ip} = n_{ip,point} + N_{motion} \cdot W_{eff} \quad , \tag{28}$$

where $W_{eff} = 2$ is the effective PSF width, consistent with the static point-source baseline.

This model naturally degenerates to the static point-source value when $N_{motion} = 0$, and increases strictly and monotonically with image motion. For small N_{motion}, the model slightly overestimates the covered area due to the overlap between the PSF and the swept region, which constitutes a conservative estimate and does not bias the visibility conclusion toward optimism.

2.3.4. Noise Model

The primary noise sources in space-based optical detection include signal photon shot noise, sky background shot noise, dark current noise and readout noise. All noise sources are statistically independent and follow Gaussian distributions. The total noise variance equals the sum of the variances of each component [34].

Signal photon shot noise: The arrival of photons follows a Poisson distribution, and its variance equals the mean value: $\sigma_{shot}^2 = S$.

Sky background shot noise: The average number of electrons generated by deep-space background (zodiacal light, galactic light, etc.) is $B = Kn_{ip}\tau$, where K denotes the sky background count rate. Its variance satisfies $\sigma_{sky}^2 = B = Kn_{ip}\tau$.

Dark current noise: It originates from thermal excitation inside the detector. The average number of dark electrons is $I_{dark}n_{ip}\tau$, and its variance satisfies $\sigma_{dark}^2 = I_{dark}n_{ip}\tau$.

Readout Noise: It is introduced by signal amplification and analog-to-digital conversion, and its variance is proportional to the number of pixels: $\sigma_R^2 = R_N^2 n_{ip}$, where R_N denotes the root-mean-square value of readout noise.

Among the above parameters, K, I_{dark} and R_N are determined by the detector model selection and operating temperature. This paper refers to the detector parameters of the Andor Balor adopted by Pineau [35] et al. for space surveillance applications: K = 10 $e^{-}\cdot s^{-1}\cdot pixel^{-1}$, I_{dark} = 0.03 $e^{-}\cdot s^{-1}\cdot pixel^{-1}$, R_N = 7.0 e^{-} rms. This set of parameters is representative and applicable to most scientific-grade CMOS/CCD sensors. Accordingly, the standard deviation of total noise is expressed as

$$N = \sqrt{\sigma_{shot}^2 + \sigma_{sky}^2 + \sigma_{dark}^2 + \sigma_R^2} = \sqrt{S + n_{ip}[(K + I_{dark})\tau + R_N^2]}, \quad (29)$$

2.3.5. SNR and Detection Threshold

The signal-to-noise ratio (SNR) is defined as the ratio of the number of signal photoelectrons to the standard deviation of total noise:

$$SNR = \frac{S}{N} = \frac{S}{\sqrt{S + n_{ip}[(K + I_{dark})\tau + R_N^2]}} \quad (30)$$

The SNR defined in Equation (30) corresponds to an unweighted integrated SNR: the total signal photoelectrons summed over all n_{ip} covered pixels divided by the standard deviation of the total noise over the same pixel set, with no amplitude weighting applied to individual pixels.

In space target detection, a minimum acceptable SNR threshold SNR_{min} is generally specified, which requires a trade-off between detection probability and false alarm rate. Under the independent Gaussian noise assumption stated in Section 2.3.4, the detection performance of this integrated SNR statistic can be evaluated by

$$P_d = Q\left(Q^{-1}(P_{fa}) - SNR\right) \quad (31)$$

where Q(·) denotes the right-tail probability of the standard normal distribution. With $SNRmin$ = 6, this gives P_d = 0.89 at P_{fa} = 10^{-6}, 0.96 at 10^{-5} and 0.99 at 10^{-4} per resolved detection cell. Because Equation (30) includes the signal shot-noise term in the variance, the variance under the signal hypothesis slightly exceeds that under the noise-only hypothesis; the equal-variance expression above therefore yields a conservative lower bound on P_d.

Since observations are cued by a predicted target position, the detector is applied within a small local window; a blind full-frame search over N independent cells would require P_{fa}/N per cell and a correspondingly higher SNR. It should be noted that if a weighted matched filter or a local single-pixel peak detector were adopted, the detection threshold would require recalibration based on the signal distribution and PSF energy

concentration; such detection modes are not applied in the present work. Accordingly, the detection capability criterion is defined as

$$B_{detect} = \begin{cases} 1, SNR \geq SNR_{min} \\ 0, SNR < SNR_{min} \end{cases}, \tag{32}$$

2.4. Definition of Comprehensive Visibility

The comprehensive visibility flag is jointly determined by the three-layer criteria above via logical AND operation:

$$B_{total}(t) = B_O(t) \wedge B_{photo}(t) \wedge B_{detect}(t), \tag{33}$$

This progressive logical structure guarantees the scientific rigor of the comprehensive criterion. A target is identified as "effectively visible" only when it simultaneously satisfies three conditions: geometric visibility, sufficient brightness, and reliable detectability by the sensor.

3. Simulation Scenarios and Parameter Settings

To verify the validity of the proposed comprehensive visibility model, we construct the overall framework of the simulation experiments, which includes the definition of the observation constellation, targets, optical sensors, and simulation operation rules. All parameters are selected based on the engineering specifications of existing space-based surveillance satellites and optical payloads.

3.1. Simulation Setup

This paper adopts a time-discretized stepping full-link visibility simulation framework to perform quantitative determination of space target space-based observation visibility moment by moment with a fixed step size of 5 s within a 6-day simulation period. For celestial position calculation, the Meeus astronomical algorithm model corrected by the IAU1976 precession is employed to solve the instantaneous ecliptic coordinates of the Sun and the Moon respectively, which are uniformly transformed into the J2000.0 geocentric mean equator inertial coordinate system (ECI) through the precession rotation matrix, ensuring a consistent coordinate datum across the full link. All simulations start from the epoch of 00:00 UTC on 1 June 2026. The right ascension of the ascending node of the reference orbital plane is set to 0°, corresponding to an LTAN of approximately 07:26 at the start epoch. The orbit propagation of both observation satellites and space targets adopts the Keplerian two-body analytical method. Based on the mean motion formula, the linear evolution of the mean anomaly over time is analytically calculated, and the in-orbit-plane coordinates are converted into instantaneous position and velocity vectors under J2000 ECI through three Euler rotation transformations of the right ascension of the ascending node, orbital inclination, and argument of perigee.

On this basis, a three-stage progressive visibility determination mechanism of geometric constraint—photometric constraint—detector constraint is constructed: First, the conical shadow model is used to determine the Earth shadow state of the target, and Earth occlusion verification is completed in combination with the line-sphere intersection algorithm. Meanwhile, Sun and Moon avoidance angle constraints are introduced, and the four conditions together constitute the geometric visibility criterion. For moments satisfying geometric visibility, the phase angle formed by the target, observation satellite and Sun is further calculated, and the hybrid diffuse-specular photometric model is adopted to solve the optical scattering characteristics of the target, so as to obtain the target apparent magnitude. Finally, combined with optical system parameters and the relative

motion velocity of the target, the image motion smear and the number of covered imaging pixels are calculated. An SNR model including signal photoelectrons, background noise, dark current and readout noise is established, and the comprehensive visibility result is output with the apparent magnitude threshold, SNR threshold and image motion smear threshold as joint criteria. For constellation-level statistics, an OR-logic merging rule is adopted: an epoch is recorded as comprehensively visible if at least one satellite in the constellation satisfies the criterion. Epochs with multiple simultaneously visible satellites are counted only once to avoid duplicate statistics. The specific flow chart is shown in Figure 6.

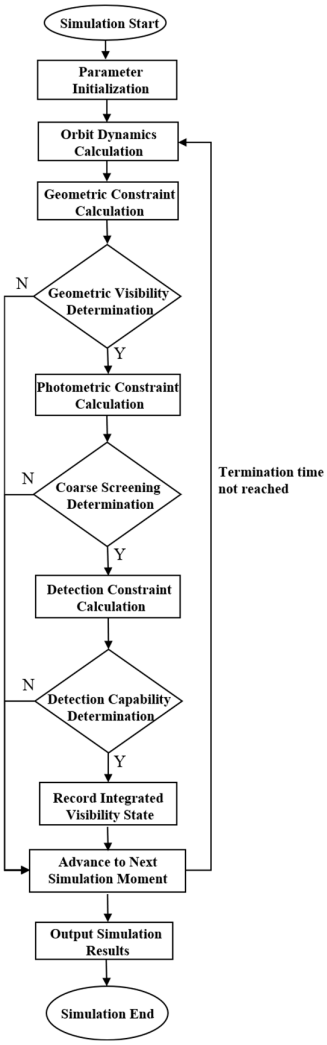

Figure 6. Simulation Flowchart.

3.2. Constellation Configuration

A low-Earth-orbit sun-synchronous surveillance constellation is selected as the observation platform in this simulation. As a typical orbit configuration for space-based optical surveillance, a sun-synchronous orbit maintains a fixed local time of the ascending node (LTAN) for each orbital plane over long durations: the secular precession rate of the right ascension of the ascending node (RAAN) approximately matches the Earth's mean orbital revolution rate around the Sun. This characteristic ensures stable illumination geometry for each orbital plane.

Four observation satellites are deployed in the constellation, distributed across four separate sun-synchronous orbital planes with a uniform RAAN spacing of 90°. This evenly distributed multi-plane configuration enables multi-temporal coverage and high revisit frequency for target sky regions, suitable for wide-area space target surveillance tasks. The detailed orbital parameters are listed in Table 1.

Table 1. Orbit Parameters of the Observation Constellation.

Parameter	Value
Orbital altitude	800 km
Semi-major axis	7171 km
Eccentricity	0
Inclination	98.6°
RAAN spacing	90°
Argument of perigee	0°
Initial mean anomaly	0°

3.3. Targets Setup

The orbital altitude of space objects is a core factor affecting observation performance. Objects in different orbits exhibit significant differences in relative motion characteristics, apparent brightness, occultation probability and other aspects. To conduct a comparative analysis, this paper selects two typical types of space objects, GEO targets and LEO targets, for simulation. Both types adopt near-circular orbits and represent the key surveillance targets in the current aerospace field.

GEO objects remain nearly stationary relative to the ground, and the geostationary orbit serves as the primary deployment orbit for communication, navigation, and early warning satellites. LEO objects operate at low orbital altitudes with high velocities and frequent orbital maneuvers, including remote sensing satellites, on-orbit platforms, space debris, and other objects. These two categories are highly representative. The orbital parameters of the observation targets are listed in Table 2.

Table 2. Orbital Parameters of Observation Targets.

Parameter	GEO Target 1	GEO Target 2	LEO Target 1	LEO Target 2
Semi-major Axis	42,164 km	42,164 km	6871 km	7371 km
Orbital Altitude	35,786 km	35,786 km	500 km	1000 km
Orbital Eccentricity	0	0	0	0
Orbital Inclination	0.1°	0.1°	87°	87°
Right Ascension of Ascending Node	120°	60°	90°	90°
Argument of Perigee	0°	0°	0°	0°
Initial Mean Anomaly	0°	0°	0°	0°

3.4. Sensor Setup

Visible light optical imaging payloads are adopted in the simulation, with parameters referring to typical specifications of commercial small-satellite optical surveillance payloads [35]. Considering the imaging characteristics of distant point-like GEO targets and high-speed moving LEO targets, point-source imaging mode is applied for GEO target detection, while streak imaging mode is adopted for LEO target detection. Parameters related to the optical system, detector and detection threshold are summarized in Table 3. The observation operates in inertial staring mode: the optical axis remains inertially aligned with the target sky region during a single exposure, and no active target tracking is performed, which is consistent with the image motion calculation model in

Section 2.3. It should be noted that this work focuses on the intrinsic coupling law between orbital geometry, photometric characteristics and detection performance. An idealized flexible-pointing assumption is adopted: the sensor can be reoriented to the target sky region between exposures, and no field-of-view boundary or attitude slew constraint is imposed. This assumption will overestimate the actual visibility duration to a certain extent. The engineering constraints such as attitude scheduling and field-of-view limitation will be introduced in follow-up work for more practical analysis.

Table 3. Sensor Parameters.

Parameter Category	Parameter Name	Value/Description
Optical System	Aperture Diameter	0.15 m
	Focal Length	0.42 m (F-number = 2.8)
	Pixel Size	12 μm
	Optical Transmittance	0.8
Imaging Mode	Exposure time for GEO Targets	0.1 s
	Exposure time for LEO Targets	0.025 s
Detector	Quantum Efficiency	61%
	Readout Noise	7 e^- rms
	Dark Current	0.03 $e^- \cdot s^{-1} \cdot pixel^{-1}$
	Sky Background Count Rate	10 $e^- \cdot s^{-1} \cdot pixel^{-1}$
Environment & Threshold	Background Radiance	2×10^{-3}
	Limiting Apparent Magnitude	13.5
	SNR Detection Threshold	6

4. Simulation Results and Analysis

Based on the foregoing theoretical analysis and simulation configurations, this paper systematically analyzes the visibility laws of the space-based space object sensing constellation for two typical types of space targets (GEO and LEO) from three dimensions: temporal distribution of visibility, variation characteristics of core physical quantities, and contribution degree of observation constraints.

4.1. Analysis of Temporal Characteristics of Visibility

Temporal visibility serves as the fundamental basis for evaluating the distribution of observation windows and supporting observation mission planning. In this simulation, geometric visibility is defined as the line of sight between the target and observation satellite being unobstructed by the Earth, the solar avoidance angle ≥30°, the moon avoidance angle ≥10°, and the target residing in the solar illumination region. Comprehensive visibility is defined as the condition where, on the premise of geometric visibility, the apparent magnitude of the target ≤13.5 and the imaging SNR ≥6. The comparative temporal visibility results of the two types of targets are illustrated in Figure 7.

As shown in Figure 7a,b, the visibility of GEO targets exhibited a distribution characteristic of long arcs and sparse discontinuities. Within the simulation period, GEO Target 1 presented 20 comprehensive visibility windows with a maximum visible duration of up to 30.25 min, while GEO Target 2 presented 20 comprehensive visibility windows with a maximum visible duration of up to 30.08 min. The orbital angular velocity of the GEO target is approximately 7.29×10^{-5} rad/s, while the orbital angular velocity of the LEO observation satellite at an altitude of 800 km is around 1.04×10^{-3} rad/s. Despite the high orbital rate of the observer, the long slant range 3.6×10^4 km to the GEO target yields a low line-of-sight angular rate, enabling long geometric visibility arcs with rare Earth occultation. Nevertheless, comprehensive visibility is a strict subset of

geometric visibility, interrupted when illumination, photometric or SNR criteria fail. This behavior arises from the refined penumbra and Earth-shadow model, which breaks potential ultra-long illumination arcs and limits the maximum single-pass duration.

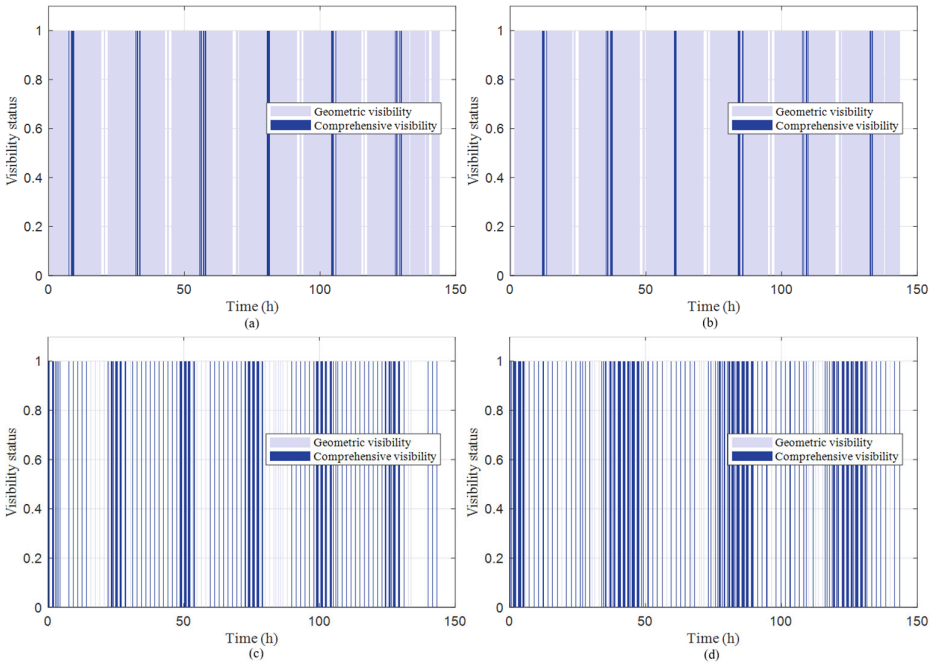

Figure 7. Time-series Diagram of Visibility Over the Entire Period. (**a**) GEO1 visibility time series. (**b**) GEO2 visibility time series. (**c**) LEO1 visibility time Series. (**d**) LEO2 visibility time series.

As illustrated in Figure 7c,d, the visibility of LEO targets exhibited characteristics of short sharp peaks and high-density discreteness, in marked contrast to GEO targets. Within the simulation period, LEO Target 1 presented 125 comprehensive visibility windows with a minimum visible duration of 0.17 min, and LEO Target 2 produces 141 windows with a maximum duration of 71.33 min. The relative motion between the LEO target and observation satellite is intense. The orbital angular velocity of the LEO target at an altitude of 500 km is approximately 1.16×10^{-3} rad/s. Similar orbital altitudes produce high relative speeds of several km/s and a much higher line-of-sight angular rate; the target quickly crosses the field of view and undergoes frequent occultation, forming abundant short windows. While short windows dominate statistically, favorable orbital-illumination phasing can continuously satisfy all constraints and create the observed long-duration outlier.

4.2. Analysis of Variation Characteristics of Target Apparent Magnitude and SNR

Figure 8a,b,e,f present the apparent magnitude variation curves of GEO Target 1, GEO Target 2, LEO Target 1 and LEO Target 2 during the observation period, respectively. In the figures, the red dashed line denotes the limiting magnitude $m_{\lim} = 13.5$, and the solid blue lines represent the temporal evolution of the target apparent magnitude. The apparent magnitude of GEO targets fluctuated within a narrow range and exhibited periodic oscillations consistent with the orbital period, varying roughly from magnitude 13 to 19. The brightness satisfied the photometric criterion for only a small fraction of the observation duration. During most of the observation period, the received reflected light was insufficient owing to the long observation distances and unfavorable Sun–target–observer phase angles, leaving the apparent magnitude above the limiting threshold. In contrast, the apparent magnitude of LEO targets underwent high-frequency violent

oscillations ranging from magnitude 2 to 15, with a peak-to-valley difference exceeding 13 magnitudes. This phenomenon originated from the rapid evolution of the relative geometry between LEO targets and the observation satellites. The continuous rapid sweep of the solar phase angle within a short timeframe, coupled with the angular sensitivity of the specular reflection components on the target surface, generated numerous sharp peaks and troughs on the magnitude curve.

The corresponding SNR curves in Figure 8c,d,g,h further revealed the fundamental differences in detection performance between the two target categories. The SNR of GEO targets varied periodically in synchronization with the apparent magnitude and generally featured broad peaks with maximum values above 8; the SNR only dropped below the detection threshold of 6 during orbital arcs with maximum target range and unfavorable phase angles. Although specular reflection produced extremely high SNR spikes for LEO targets that far surpassed those of GEO targets (with peak values exceeding 600), the SNR remained concentrated around 100 for most time intervals. The above results indicated that the photometric criterion only accomplished coarse screening at the level of target brightness. Particularly for LEO targets, the coupling effect of the rapid variation in geometric configuration and short exposure time resulted in a large number of periods where targets were photometrically visible but their SNR was unusable, ultimately making the comprehensive visibility windows significantly smaller than the photometric visibility windows.

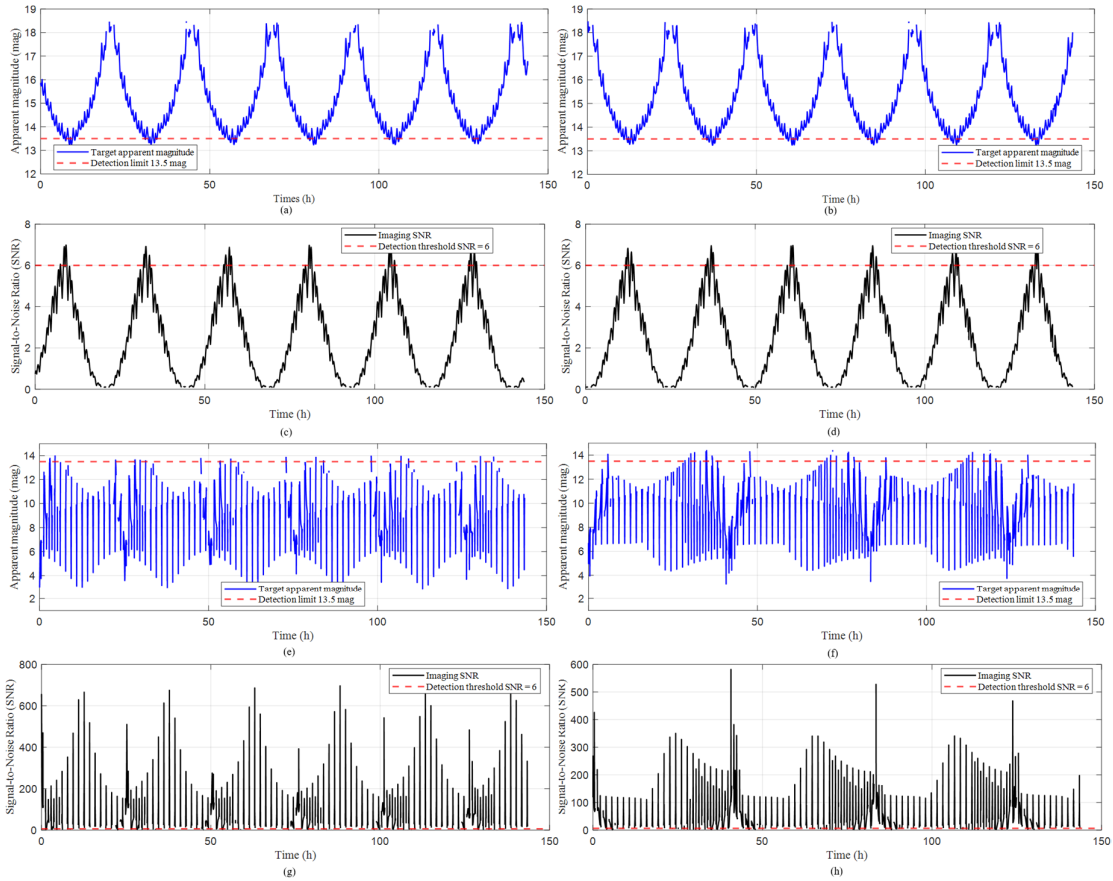

Figure 8. Variation Curves of Apparent Magnitude and Signal-to-Noise Ratio. (**a**) Global variation curve of apparent magnitude for GEO1; (**b**) Global variation curve of apparent magnitude for GEO2; (**c**) Global variation curve of SNR for GEO1; (**d**) Global variation curve of SNR for GEO2; (**e**) Global variation curve of apparent magnitude for LEO1; (**f**) Global variation curve of apparent

magnitude for LEO2; (**g**) Global variation curve of SNR for LEO1; (**h**) Global variation curve of SNR for LEO2.

4.3. Analysis of Constraint Interaction in Typical Arcs

To further reveal the mechanism underlying the difference between geometric visibility and comprehensive visibility, the time intervals of 4 h to 10 h after the start of simulation for GEO target 1 and 2 h to 8 h for LEO target 1 were selected as typical analysis arcs for magnified visualization, as shown in Figure 9a–f. The intercepted arcs clearly demonstrate the varying characteristics of target visibility status.

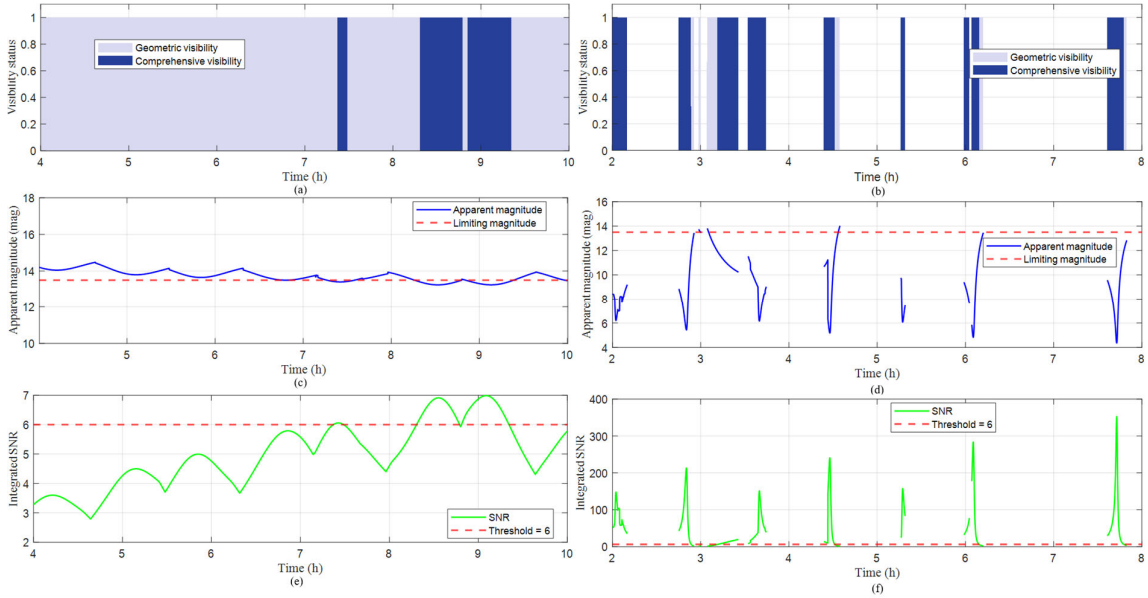

Figure 9. Analysis of Typical Arcs. (**a**) GEO1 visibility time series; (**b**) LEO1 visibility time series; (**c**) GEO1 apparent magnitude variation curve; (**d**) LEO1 apparent magnitude variation curve; (**e**) GEO1 SNR variation curve; (**f**) LEO1 SNR variation curve;

For GEO targets (Figure 9a,c,e), within the long-duration visibility window from 4 h to 10 h, the comprehensive visibility states are relatively concentrated. Correspondingly, the apparent magnitude curve dropped below the limiting magnitude threshold of 13.5, and the SNR exceeded the detection threshold of 6. In contrast, the geometric visibility windows of LEO targets (Figure 9b,d,f) are distributed as discrete short arcs. Within each arc, only partial time intervals simultaneously satisfied the two constraints: apparent magnitude ≤ 13.5 and SNR ≥ 6. As a result, the comprehensive visibility windows are markedly shorter than the geometric visibility windows. The apparent magnitude curve of LEO targets fluctuated drastically; specular reflection caused sharp magnitude drops in certain periods, which in turn produced prominent SNR spikes. Nevertheless, detection requirements could not be satisfied for most of the time due to insufficient signal accumulation or unfavorable phase angles. By comparing the visibility evolution characteristics of the two types of targets, it can be concluded that the loss of visibility for GEO targets mainly arose from long observation ranges and deteriorated phase angles induced by orbital periodicity. For LEO targets, however, the coupling effect of rapidly varying relative geometric configurations and short exposure times led to highly fragmented visibility windows. The proposed comprehensive criterion can accurately identify valid time intervals in which targets are truly detectable.

4.4. Constraint Rejection Analysis

To clarify the limiting factors of target visibility, two sets of statistics are presented from complementary perspectives: sequential rejection fractions of the screening pipeline, and independent contribution weights of each constraint.

4.4.1. Sequential Rejection Fractions

The visibility assessment follows a progressive screening pipeline: geometric occultation constraint first, then photometric magnitude constraint, and finally SNR detection constraint. The rejection fraction of each stage represents the proportion of epochs at which targets are rejected at that step of the sequence. This statistic reflects the actual interception distribution of the engineering screening workflow, and its numerical value depends on the order of the filters.

Figure 10 classifies the full-period simulation data into four mutually exclusive groups: geometrically invisible, photometrically unsatisfied (geometrically visible but apparent magnitude > 13.5), insufficient SNR (the first two conditions satisfied but SNR < 6), and comprehensively visible (all three conditions satisfied). The figures clearly illustrate the proportional distribution of visibility constraints for the two types of targets. For LEO targets, the distribution characteristics are notably different. For LEO Target 1, geometric invisibility periods accounted for as high as 73.29% of the total time, photometric non-compliance periods accounted for only 0.24%, insufficient SNR periods accounted for 1.80%, and comprehensive visibility periods accounted for 24.66%. For GEO Target 1, geometric invisibility periods accounted for 6.72%, photometric non-compliance periods accounted for 86.00%, insufficient SNR periods account for 2.22%, and the final comprehensive visibility periods accounted for 5.07%. This distribution reveals that the dominant limiting factor for GEO targets in this sequential screening pipeline is the photometric constraint. Insufficient target brightness causes most geometrically visible intervals to fail the photometric screening, while the SNR constraint exerts a relatively weak impact and only takes effect in a tiny fraction of marginal time intervals. By comparing the constraint distributions of the two target types under this sequential screening rule, the key factors limiting their visibility in the practical screening workflow are clearly identified: the core limiting factor for GEO targets is insufficient reflected brightness, whereas LEO targets are mainly constrained by geometric line-of-sight conditions and inadequate signal accumulation.

4.4.2. Independent Constraint Contributions

To quantify the marginal limiting effect of each constraint independent of the screening order, a single-constraint removal method is adopted. Let $V(S)$ denote the fraction of epochs at which at least one observing satellite simultaneously satisfies all constraints in subset $S \subseteq \{g, p, s\}$ (geometric, photometric, SNR). The baseline $V(\{g,p,s\})$ coincides exactly with the comprehensively visible fraction in Section 4.4.1. Each constraint is removed separately, and the increment $(V(S \setminus \{c\}) - V(S)$ in comprehensive visibility rate is calculated to characterize the relaxation gain of that constraint. This metric is order-independent and quantifies the marginal rejection effect of each constraint when the other two remain active. The three gains are not additive, since constraints interact; they should be interpreted as marginal contributions rather than additive weights.

https://doi.org/10.3390/aerospace13121106

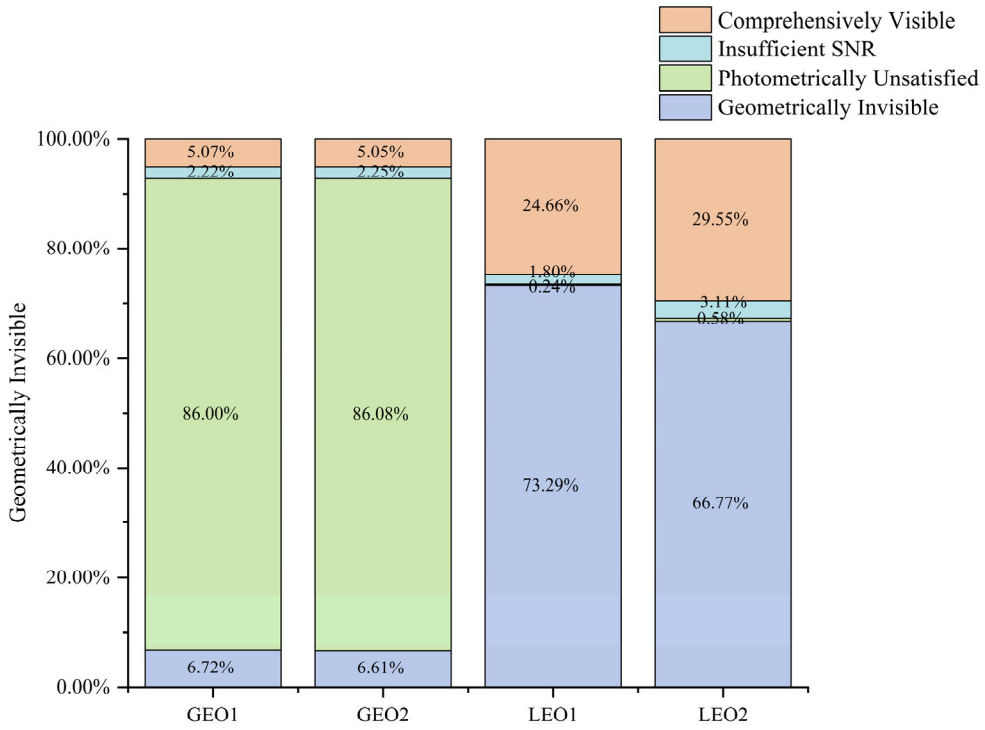

Figure 10. Sequential Rejection Fraction.

Figure 11 shows the leave-one-out contribution of geometric, photometric and SNR constraints. For GEO targets (Figure 11a,b), geometric constraints contribute nearly 0%, which means that at epochs rejected by geometry, the photometric or SNR constraint would also reject the target, so relaxing geometry alone creates no additional comprehensively visible epoch The marginal limiting effect is dominated by the SNR constraint, followed by the photometric constraint. This ranking differs from the sequential statistics in Section 4.4.1 for two reasons: first, the sequential pipeline is order-sensitive and applies the photometric threshold before the SNR judgement, so most epochs are intercepted by photometry before SNR is even evaluated; second and more fundamentally, the two statistics answer different questions—the sequential fractions describe where epochs are rejected in a fixed evaluation order, whereas the leave-one-out gains describe how many additional epochs would become visible if one constraint were relaxed while the others remain active. For LEO targets (Figure 11c,d), geometric constraints dominate the marginal limiting effect, with contribution values of 54.99% and 48.61%, respectively. The photometric constraint has almost no restrictive effect on LEO targets, and SNR imposes only a minor limitation.

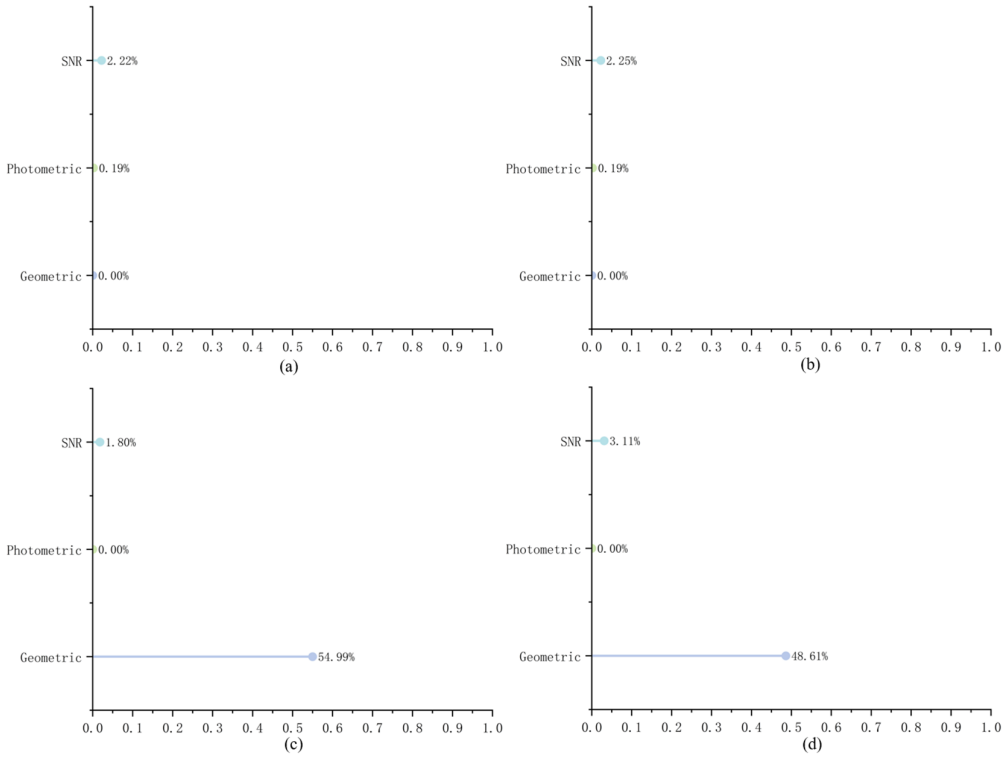

Figure 11. Contribution Analysis. (**a**) GEO1 Contribution Analysis. (**b**) GEO2 Contribution Analysis. (**c**) LEO1 Contribution Analysis. (**d**) LEO2 Contribution Analysis.

4.5. Geometric Model Benchmarking Validation

To verify the correctness and physical consistency of the geometric visibility model established in this paper, the high-precision aerospace simulation software STK 12.2 is adopted as the benchmark verification tool. The verification scenario is fully consistent with the simulation settings in the preceding section: four LEO observation satellites perform continuous 6-day observation of LEO Target 1, with completely unified orbital parameters and coordinate reference frames. Comparative analysis was carried out from three dimensions: window temporal distribution, number of windows, and cumulative visible duration. Figure 12 presents the temporal comparison results of geometric visibility windows for LEO Target 1 observed by the four satellites. Qualitatively, the visibility windows derived from the proposed model and the STK benchmark maintain fully consistent occurrence periods, repetition rhythms and overall spatiotemporal distribution patterns. This high degree of matching in distribution law confirms that the orbit propagation algorithm, celestial position calculation and line-of-sight geometric logic adopted in this paper are free from systematic deviations. More critically, all geometrically visible epochs output by the proposed model fall strictly within the visibility window range of STK, and no false-positive visibility windows exclusive to the proposed model are observed. This strict subset relationship further proves that the geometric judgment logic of our model is rigorous and self-consistent, with no missed occultation or erroneous visibility judgment.

Quantitative comparison results show that all geometric visible moments output by the proposed model for the four satellites fall within the visibility window range of STK, and there are no false positive visibility windows unique to the model. Taking Sat2 as an example, the cumulative geometric visible duration of the proposed model is 20.49 h, corresponding to 41 visibility windows; the cumulative visible duration of the STK benchmark is 23.92 h, corresponding to 28 visibility windows. The overlapping visible

duration of the two is 20.49 h, while the STK-exclusive visible duration is 3.42 h. Sat1, Sat3 and Sat4 follow the same pattern: the overlapping visible duration exactly equals the total visible duration of the proposed model, and the STK-exclusive visible durations are 2.29 h, 1.63 h and 4.30 h respectively. The shorter cumulative duration and more fragmented windows of the proposed model stem from its stricter engineering constraint settings for optical surveillance.

In summary, the STK benchmark comparison verifies the correctness of the underlying orbit dynamics and basic geometric occultation logic of our model. On this basis, the stricter engineering constraints embedded in our model produce more conservative visibility results that are closer to actual optical detection conditions, which lays a reliable geometric foundation for the subsequent photometric and detection performance layers of the comprehensive visibility framework.

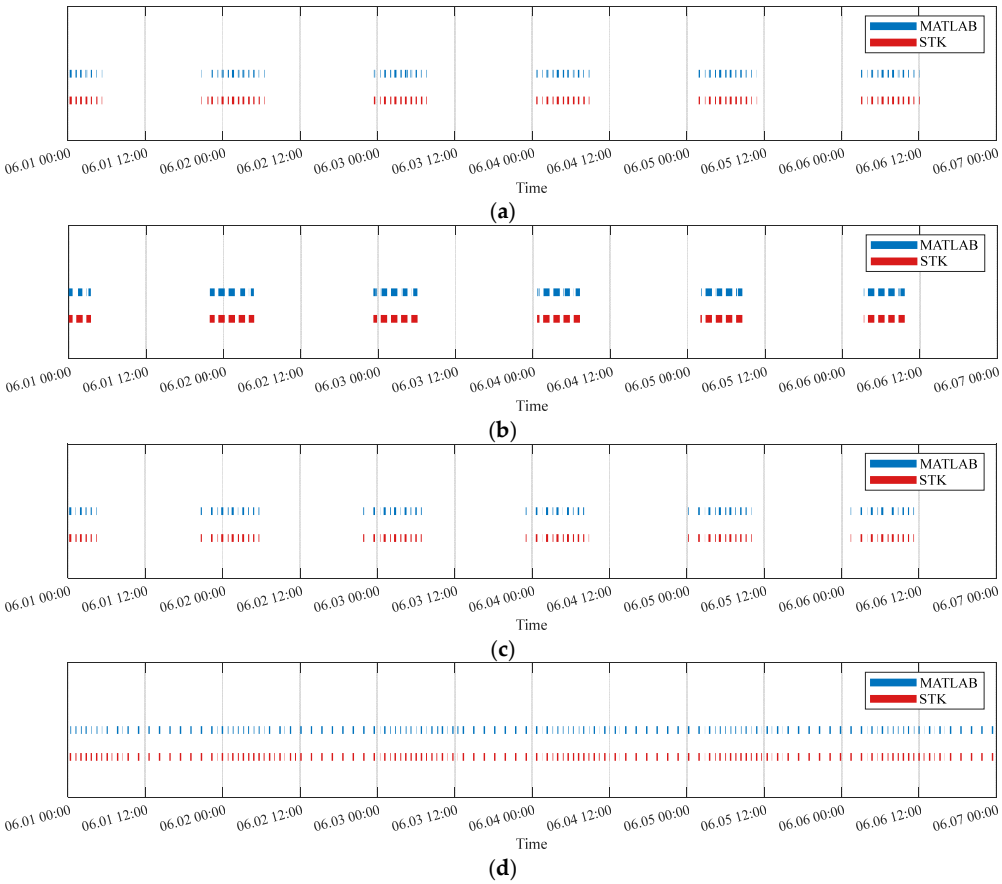

Figure 12. Temporal comparison of geometric visibility windows. (**a**) Visibility windows of LEO1 observed by Sat1. (**b**) Visibility windows of LEO1 observed by Sat2. (**c**) Visibility windows of LEO1 observed by Sat3. (**d**) Visibility windows of LEO1 observed by Sat4. Software version: MATLAB R2022b.

4.6. Parameter Sensitivity Analysis

To quantify the influence law of system design parameters and target optical characteristics on the comprehensive visibility of space-based space target observation, single-parameter sensitivity analysis was carried out based on the aforementioned simulation model. Centered on the benchmark simulation parameters, nine parameters were traversed within the reasonable engineering value range, including optical aperture, hemispherical reflectance, specular reflection weight, SNR detection threshold, read noise, target cross-sectional area, exposure time, surface roughness, and quantum efficiency. The

comprehensive visibility rate was taken as the core evaluation index. For the scans of optical aperture and exposure time, the limiting magnitude threshold is dynamically updated in accordance with the photometric definition, to avoid the magnitude prefilter artificially masking the detection performance gain from parameter optimization. Based on Pogson's magnitude law, the limiting magnitude scales with the total collected optical energy, which is proportional to the aperture area and exposure time. The dynamic correction formulas are given as follows:

For optical aperture variation: $m_{\lim}(D) = m_{\lim,0} + 2.5\lg\left(\left(\frac{D}{D_0}\right)^2\right)$; For exposure time variation: $m_{\lim}(\tau) = m_{\lim,0} + 2.5\lg\left(\left(\frac{\tau}{\tau_0}\right)^2\right)$, where D_0 = 0.15 m, τ_0 = 0.1 s and $m_{\lim,0}$ = 13.5 denote the baseline aperture, baseline exposure time for point-source mode, and the corresponding baseline limiting magnitude, respectively.

Meanwhile, for the surface roughness parameter, its influence on the fluctuation amplitude of the target relative irradiance was additionally analyzed. The analysis covered two GEO targets and two LEO targets, and the results are shown in Figure 13. The results showed that the target hemispherical reflectance and cross-sectional area had the most significant effect on improving the comprehensive visibility rate of GEO targets, following an approximately linear growth law. Optical aperture and quantum efficiency had a certain effect on visibility rate improvement in the low value range, and tend to be flat after exceeding the critical value. The increase in specular reflection weight had no effect on LEO targets, but led to an approximately linear decrease in the comprehensive visibility rate of GEO targets, and its influence intensity on GEO targets was significantly higher than that on LEO targets. The influence of SNR detection threshold in the value range of 4–6 and exposure time in the range of 0.00–0.08 s on the comprehensive visibility rate was extremely weak, and the curves remained basically horizontal. Surface roughness mainly affects the temporal fluctuation characteristics of the target relative irradiance. With the increase in surface roughness, the fluctuation amplitude of the relative irradiance of each target showed a slow downward trend and gradually stabilized, and the scattering characteristics of the target gradually approached a Lambertian diffuse reflector.

Overall, target hemispherical reflectance, cross-sectional area and specular reflection weight are the most sensitive parameters affecting comprehensive visibility, while the influence of SNR detection threshold and exposure time is relatively weak. There are differences in parameter sensitivity of targets with different orbit types: LEO targets have a more significant response to the smear pixel threshold, while GEO targets are more sensitive to changes in specular reflection weight. The above sensitivity analysis results reflect the action intensity and variation law of each parameter, and can provide quantitative basis for parameter optimization design of space-based optical surveillance systems, target detection capability evaluation and observation mission planning.

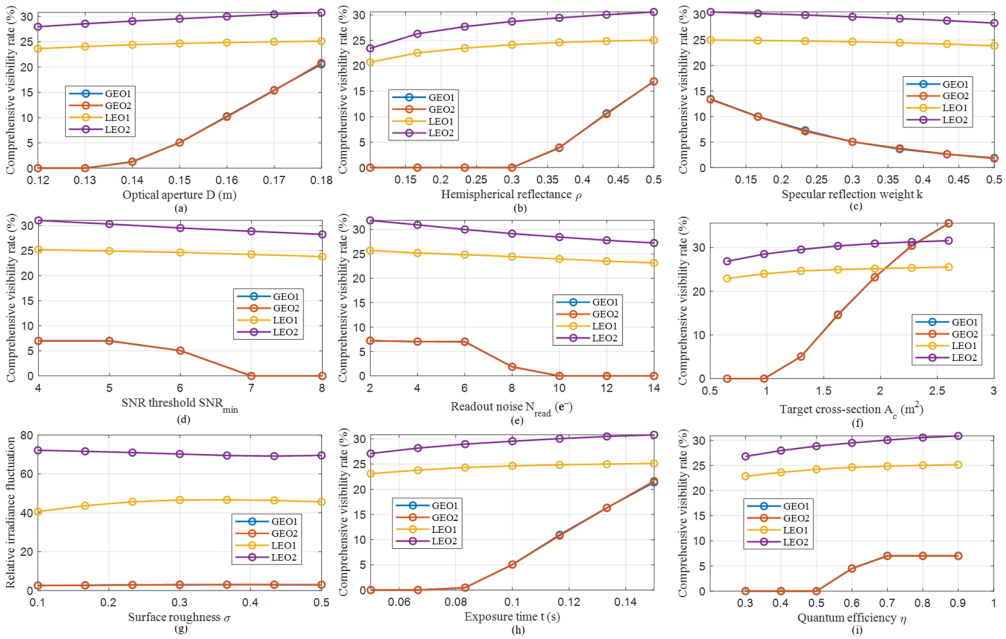

Figure 13. Sensitivity analysis. (**a**) Optical aperture. (**b**) Hemispherical reflectance. (**c**) Specular reflection weight (**d**) SNR threshold. (**e**) Readout noise. (**f**) Target cross-section. (**g**) Surface roughness. (**h**) Exposure time. (**i**) Quantum efficiency.

5. Conclusions

To assess constellation-level detectable observation opportunities for GEO and LEO targets, we construct a three-layer progressive comprehensive visibility analysis model that integrates geometry, photometry, and detection performance. The model decomposes the optical detection of space targets into three successive physical stages subject to sequential constraints: line-of-sight condition, signal energy intensity, and SNR confidence. Quantitative judgment is achieved via a logical AND operation. This model effectively addresses the limitations of traditional methods that neglect signal attenuation, noise coupling, and practical detection thresholds. It better reflects the real physical process of space-based optical detection and enables more accurate determination of the actual detectability of space targets.

Simulation results demonstrate that the proposed model can effectively distinguish between geometric and comprehensive visibility and accurately identify the bottleneck constraints for targets in different orbits. For GEO targets, the limiting effects of constraints exhibit distinct characteristics under two analytical perspectives: in the sequential screening pipeline, the photometric magnitude cutoff contributes to the majority of rejections as the first-stage coarse filter, whereas from the perspective of single-constraint marginal contribution, the relaxation of the SNR threshold yields the largest visibility gain and represents the more fundamental performance bottleneck. For LEO targets, geometric occlusion remains the dominant limiting factor under both statistical perspectives: it accounts for the largest proportion of rejections in the sequential screening pipeline and also produces the most substantial visibility improvement when the constraint is removed, while SNR serves as a secondary limiting factor. This method can provide more accurate quantitative support for observation mission planning, constellation configuration design, and the optimization of detection resource scheduling in space-based optical surveillance systems.

The proposed model employs engineering approximations in the selection of the phase function, Earth shadow model, and noise parameters. Future work can introduce

refined BRDF models incorporating the actual surface materials and structural features of targets to improve photometric accuracy. A penumbral illumination attenuation model can also be incorporated to further improve the accuracy of Earth shadow determination. In addition, by integrating multi-sensor cooperative detection mechanisms, the model can be extended to constellation-level joint detection scenarios, thereby providing better support for complex space-based object surveillance missions.

Author Contributions: Investigation, J.W.; Writing—Original Draft Preparation, J.W.; Methodology, J.W.; Supervision, D.L.; Writing—Review and Editing, D.L. All authors have read and agreed to the published version of the manuscript.

Funding: This research was funded by Beijing Natural Science Foundation, grant number L252019.

Data Availability Statement: The data, sample code and test cases presented in this study are available from the corresponding author upon reasonable request.

Conflicts of Interest: The authors declare no conflicts of interest.

References

1. Zhang, Y.N.; Li, J.Z.; Sun, J.Q.; Zhu, Y. *Intelligent Detection and Sensing of Space-Based Space Targets*; Science Press: Beijing, China, 2024; pp. 1–8. (In Chinese)
2. Wang, B.C.; Li, S.; Mu, J.Z.; Hao, X.L.; Zhu, W.S.; Hu, J.Q. Research Advancements in Key Technologies for Space-Based Situational Awareness. *Space Sci. Technol.* **2022**, *2022*, 9802793. https://doi.org/10.34133/2022/9802793.
3. Du, X.; Geng, W.; Zhao, J.; Ma, Z. *Fundamentals of Space Situational Awareness*; National Defense Industry Press: Beijing, China, 2017; pp. 65–72. (In Chinese)
4. Hu, Q.Y.; Guo, J.; Liu, D.S. A distributed space target constellation task planning method based on adaptive genetic algorithm. *Sensors* **2025**, *25*, 5485. https://doi.org/10.3390/s25175485.
5. Wang, S.Z.; Zhu, J.; Liu, T.X. A weighted optimization method for constellation configuration for large-scale LEO surveillance missions. *J. Phys. Conf. Ser.* **2026**, *3240*, 012046. https://doi.org/10.1088/1742-6596/3240/1/012046.
6. Stokes, G.; Vo, C.; Sridharan, R.; Sharma, J. The Space-Based Visible Program. In Proceedings of the Space 2000 Conference and Exposition, Long Beach, CA, USA, 19–21 September 2000. https://doi.org/10.2514/6.2000-5334.
7. Lan, C.Z. Modeling and detecting capability analysis of space-based space object optical observation system. Ph.D. Thesis, PLA Information Engineering University, Zhengzhou, China, 2009. (In Chinese)
8. Liu, Y. Mission planning and control based on multiple micro-nano satellites for space target observation. Master's Thesis, Harbin Institute of Technology, Harbin, China, 2023. (In Chinese)
9. Han, C.; Zhang, Y.J.; Bai, S.Z.; Sun, X.C.; Wang, X.W. Novel method to calculate satellite visibility for an arbitrary sensor field. *Aerosp. Sci. Technol.* **2021**, *112*, 106668. https://doi.org/10.1016/j.ast.2021.106668.
10. Ren, C.; Li, Y.; Gao, W.; Niu, W.; Li, Y.; Tang, J.; Peng, X. Optical imaging simulation of space targets in space-based passive optical detection systems. *J. Astronaut.* **2026**, *47*, 1566–1581. (In Chinese)
11. Lan, C.Z.; Li, J.S.; Ma, S.J.; Xu, Q. Prediction and analysis of orbital target's visibility based on space-based optics observation. *Opto-Electron. Eng.* **2008**, *35*, 23–27. (In Chinese)
12. Wang, Y.P.; Niu, Z.D.; Wang, D.Y.; Huang, J.; Li, P.Y.; Sun, Q. Simulation algorithm for space-based optical observation images considering influence of stray light. *Laser Optoelectron. Prog.* **2022**, *59*, 494–501. (In Chinese)
13. Wu, X.; Mao, X.; Gong, Z.; Chen, P. Equal-probability group visibility criteria for orbit design of surveillance satellite. *Acta Astronaut.* **2026**, *239*, 113–127. https://doi.org/10.1016/j.actaastro.2025.10.074.
14. Bai, X.Z.; Chen, L. Error analysis of conjunction calculation and visible time duration prediction for space-based space surveillance. *J. Astronaut.* **2015**, *36*, 574–582. (In Chinese)
15. Wang, H.; Zhang, W. Visible imaging characteristics of the space target based on bidirectional reflection distribution function. *J. Mod. Opt.* **2012**, *59*, 547–554. https://doi.org/10.1080/09500340.2011.640951.
16. Luger, R.; Agol, E.; Bartolić, F.; Foreman-Mackey, D. Analytic light curves in reflected light: Phase curves, occultations, and non-Lambertian scattering for spherical planets and moons. *Astron. J.* **2022**, *164*, 140. https://doi.org/10.3847/1538-3881/ac4017.
17. Ai, H.; Wang, W.; Sun, Z.; Zhao, R.; Ji, Z.; Han, Y. Optical reflectance modeling and apparent magnitude analysis of low-orbit satellites under different materials. *J. Phys. Conf. Ser.* **2025**, *3169*, 012018. https://doi.org/10.1088/1742-6596/3169/1/012018.

18. Kessler, D.J.; Jarvis, K.S. Obtaining the properly weighted average albedo of orbital debris from optical and radar data. *Adv. Space Res.* **2004**, *34*, 1006–1012. https://doi.org/10.1016/j.asr.2003.02.030.
19. Liu, Y.; Wen, D.; Yi, H.; Yin, Q. Simulation of apparent magnitude curves of space objects. *Chin. J. Space Sci.* **2022**, *42*, 485–491. (In Chinese) https://doi.org/10.11728/cjss2022.03.210721079
20. Lu, Y. BRDF-based photometric modeling of LEO constellation satellite from massive observations. *Universe* **2024**, *10*, 215. https://doi.org/10.3390/universe10050215.
21. Pan, H.; Song, G.; Xie, L.; Zhao, Y. Detection method for small and dim targets from a time series of images observed by a space-based optical detection system. *Opt. Rev.* **2014**, *21*, 292–297. https://doi.org/10.1007/s10043-014-0044-7.
22. Liu, J.; Yu, F.; Yang, Y.; Wu, Y. Modular detection framework for space targets in short-exposure imagery. *Adv. Space Res.* **2026**, *77*, 11098–11109. https://doi.org/10.1016/j.asr.2026.01.003.
23. Li, J.; Dai, D.; Yu, Y.; Ma, L.; Qin, S. Refined modeling of effective visible magnitudes for optical observations of low Earth orbit satellites. *Measurement* **2026**, *266*, 120478. https://doi.org/10.1016/j.measurement.2026.120478.
24. Han, Y.; Wen, D.; Li, J.; Qiao, Z. Improved detection of multiple faint streak-like space targets from a single star image. *Remote Sens.* **2025**, *17*, 631. https://doi.org/10.3390/rs17040631.
25. Tan, J.; Yang, S.; Lei, T.; Liu, H.; Du, J.; Li, H.; Cui, Z. Faint streak-like space target detection via grayscale-similarity weighting anisotropic Gaussian kernel and directional consistency analysis. *IEEE Access* **2026**, *14*, 38129–38143. https://doi.org/10.1109/ACCESS.2026.3671198.
26. Shell, J. Optimizing orbital debris monitoring with optical telescopes. In Proceedings of the Advanced Maui Optical and Space Surveillance Technologies Conference (AMOS), Maui, HI, USA, 14–17 September 2010.
27. Campiti, G.; Brunetti, G.; Ciminelli, C. Detectability of Potentially Colliding Space Objects via Star Trackers on at-Risk Satellites. *IEEE Trans. Aerosp. Electron. Syst.* **2025**, *61*, 11489–11511. https://doi.org/10.1109/TAES.2025.3566681.
28. Clemens, S.D. On-orbit resident space object (RSO) detection using commercial grade star trackers. Master's Thesis, York University, Toronto, ON, Canada, 2019.
29. Yang, L.; Xu, C.; Zhang, Y.S. Photometric Characterization of Space Objects: From Classical BRDF Models to Data-Driven Prediction. *Aerospace* **2026**, *13*, 418. https://doi.org/10.3390/aerospace13050418.
30. Kopp, G.; Lean, J.L. A new, lower value of total solar irradiance: Evidence and climate significance. *Geophys. Res. Lett.* **2011**, *38*, L01706. https://doi.org/10.1029/2010GL045777.
31. Karttunen, H.; Kröger, P.; Oja, H.; Poutanen, M.; Donner, K.J. *Fundamental Astronomy*; Springer: Cham, Switzerland, 2017; pp. 93–109.
32. Littoriano, G.; Colombo, C.; Nastasi, A.; Falco, C. Modelling of spacecraft apparent brightness: A study on OneWeb constellation satellites. *Adv. Space Res.* **2024**, *74*, 1392–1409. https://doi.org/10.1016/j.asr.2024.04.010.
33. D'Anniballe, A.; Felicetti, L.; Hobbs, S. Preliminary analysis and design of an optical space surveillance and tracking constellation for LEO coverage. *Acta Astronaut.* **2025**, *231*, 47–63. https://doi.org/10.1016/j.actaastro.2025.02.019.
34. Lyzhof, J.; Basart, J.; Wie, B. A new terminal guidance sensor system for asteroid intercept or rendezvous missions. *Acta Astronaut.* **2016**, *119*, 147–159. https://doi.org/10.1016/j.actaastro.2015.11.019.
35. Pineau, D.; Felicetti, L. Design of an optical system for a Multi-CubeSats debris surveillance mission. *Acta Astronaut.* **2023**, *210*, 535–546. https://doi.org/10.1016/j.actaastro.2023.04.027.

Disclaimer/Publisher's Note: The statements, opinions and data contained in all publications are solely those of the individual author(s) and contributor(s) and not of MDPI and/or the editor(s). MDPI and/or the editor(s) disclaim responsibility for any injury to people or property resulting from any ideas, methods, instructions or products referred to in the content.